

**Authors Version**

# **Effects of Yttria Content on the CMAS Infiltration Resistance of Yttria Stabilized Thermal Barrier Coatings System**

Juan J. Gomez Chavez<sup>a</sup>, Ravisankar Naraparaju<sup>b</sup>, Peter Mechnich<sup>b</sup>, Klemens Kelm<sup>b</sup>, Uwe Schulz<sup>b</sup> and C.V. Ramana<sup>a\*</sup>

<sup>a</sup> University of Texas at el Paso, Department of Mechanical Engineering, El Paso, TX, 79968, USA

<sup>b</sup> German Aerospace Center (DLR), Institute of Materials Research, Cologne, 51170, Germany

\*Corresponding author: Prof., Ph.D., C.V. Ramana,  
E-mail address: [rvchintalapalle@utep.edu](mailto:rvchintalapalle@utep.edu)

Key words: CMAS, Volcanic ash, Infiltration, EB-PVD, TBC

**Journal of Materials Science & Technology 2019 (Accepted)**

# Effects of Yttria Content on the CMAS Infiltration Resistance of Yttria Stabilized Thermal Barrier Coatings System

## Abstract

The effects of  $YO_{1.5}$  doping in yttria-zirconia based TBCs against CMAS interaction/infiltration are discussed. The TBCs with an  $YO_{1.5}$  content ranging from 43 to 67 mol % (balance  $ZrO_2$ ) were produced by EB-PVD techniques. The results reveal a trend of higher apatite formation probability with the higher free  $YO_{1.5}$  available in the yttria-zirconia system. Additionally, the infiltration resistance and amount of consumed coating appears to be strongly dependent on the  $YO_{1.5}$  content in the coating. The thinnest reaction layer and lowest infiltration was found for the highest produced 67 $YO_{1.5}$  coating. Complementary XRD experiments with volcanic ash/ $YO_{1.5}$  powder mixtures with higher yttria contents than in the coatings (80 $YO_{1.5}$  and pure  $YO_{1.5}$ ) also showed higher apatite formation with respect to increasing yttria content. The threshold composition to promote apatite-based reaction products was found to be around 50 $YO_{1.5}$  in zirconia which was proved in the coatings and XRD powder experiments. An  $YO_{1.5}$ - $ZrO_2$ - $FeO$ - $TiO_2$  bearing zirconolite-type phase was formed as a reaction product for all the coating compositions which implicates that  $TiO_2$  in the melt acts as a trigger for zirconolite formation. This phase could be detrimental for CMAS/Volcanic Ash infiltration resistance since it can be formed alongside with apatite which controls or limits the amount of  $Y^{3+}$  available for glass crystallization. The Fe rich garnet phase containing all the possible elements exhibited a slower nucleation compared to apatite and its growth was enhanced with slow cooling rates. The implications of phase stability and heat treatment effects on the reaction products are discussed for tests performed at 1250 °C.

## 1.Introduction

Thermal barrier coatings (TBCs) find extensive utilization in gas turbines and aero-engine parts to protect the metallic surfaces and engine components from high temperature exposure for extended duration. The TBCs represent state of the art material systems, which are critical components of modern gas turbines allowing them to operate at temperatures higher than the melting point of Ni-based super alloys. Thus, the engine's thermal efficiency is increased significantly <sup>[1-8]</sup>. The material of selection for the TBC refractory ceramic represents 7 wt % Y<sub>2</sub>O<sub>3</sub> stabilized ZrO<sub>2</sub> (7YSZ), which is commonly produced by means of electron beam physical vapor deposition (EB-PVD) or atmospheric plasma spray (APS). These deposition techniques provide a complex network of porous features in the microstructure, which in combination with the low thermal conductivity 7YSZ produces all properties of an excellent insulator. In addition, the porous microstructure features also provide strain tolerance to the high thermal cycles that the engines are typically encountered in operation <sup>[9]</sup>. Furthermore, the current high demands in industry for more fuel-efficient gas turbines that can be operated at temperatures up to 1500 °C has brought into attention the vulnerability of TBC against high temperature corrosion related to ingestion of silicate based debris into the engine; commonly referred to as CMAS attack <sup>[3, 10, 11]</sup>. This currently represents the main technological limitation to the development of high temperature capable engines based on more sophisticated high temperature structural material systems based on ceramic matrix composites (CMC) protected with environmental barrier coatings (EBC) <sup>[11-16]</sup>. CMAS refers to the chemical composition of CaO-MgO-Al<sub>2</sub>O<sub>3</sub>-SiO<sub>2</sub>, which represent the main oxides present and their sources are dust, sand, volcanic ash, fly ash, runway debris and environmental pollution. As these debris are ingested into engines, they melt and deposit onto the TBC surfaces and consequently infiltrate into the porous features of the coatings. This infiltration generates corrosion of the 7YSZ material and also loss of the strain tolerance of the coating which produces premature coating failure <sup>[3, 10, 11, 17-20]</sup>. Special attention has been

paid to volcanic ash as a CMAS source from the unprecedented eruption of the Eyjafjallajökull volcano in 2010 in Iceland. This eruption generated a significant air traffic disruption and obligated engine manufacturers to re-consider the threats that volcanic ash concentrations pose to aviation safety<sup>[21]</sup>. Due to the serious threats that CMAS attack has on reducing TBC lifetime, significant research attention and efforts are directed to mitigate CMAS infiltration in gas turbines. One of the most successfully tested CMAS mitigation strategies involves the use of a coating material based on rare-earth (RE) zirconates or hafnates with a high RE oxide concentration (50 mol % or higher) which reacts with the molten CMAS glass inducing its crystallization into stable crystalline products such as apatite therefore, the infiltration is minimized<sup>[11, 22-35]</sup>. Therefore, it has been widely recognized that an effective CMAS reactive material must react quickly upon interaction with the glass melt and it must induce crystallization of products, which can effectively seal the porous TBC features in order to minimize CMAS infiltration. However, current studies on CMAS resistant coatings do not evaluate the effects of the different RE contents in EB-PVD coatings on their CMAS resistance. In this context, the goal of the present work is to provide a detailed investigation on the reaction kinetics of EB-PVD YSZ coatings having  $YO_{1.5}$  contents ranging from 43 to 67 mol % with respect to their volcanic ash crystallization potential. The detailed study of the influence of coating composition on the infiltration resistance presented and discussed in this paper is useful to develop strategies for effective infiltration resistance.

## **2. Materials and Methods**

### **2.1. Coating Preparation**

Yttria-zirconia coatings were prepared by EB-PVD using a jumping beam method with two evaporation sources, one matching the standard 7YSZ composition and the other one being pure  $Y_2O_3$  as done in previous studies<sup>[30]</sup>. The sample holder was positioned in

between the two crucibles in a parallel plane configuration as shown in **Figure 1a**. The produced samples exhibited an overall thickness of  $50 (\pm 3) \mu\text{m}$  and were deposited on top of previously developed 65 wt %  $\text{Y}_2\text{O}_3\text{-ZrO}_2$  coating (produced with the same jumping beam procedure as described elsewhere <sup>[30]</sup>). The used deposition power was 112 KW and the average deposition rate was about  $1.8 \mu\text{m}/\text{min}$ . Additionally, the deposition chamber temperature was set at about  $1000 \text{ }^\circ\text{C}$ , the deposition chamber pressure was set at  $4 \times 10^{-3}$  mbar and the sample holder had a set rotation of 30 RPM. The fast sample rotations were selected to produce enlarged feather arms as described in previous studies <sup>[36]</sup>. A schematic of the complete TBC system with the substrate is shown in **Figure 1b**. A 1 mm thick  $\text{Al}_2\text{O}_3$  substrate was used due to the advantages it gives to test high-temperature infiltration ( $>1250 \text{ }^\circ\text{C}$ ) which cannot be tested if standard Ni-based superalloy substrates are used. Due to the evaporation process, two clouds of different evaporated material e.g. 7YSZ and  $\text{Y}_2\text{O}_3$  are produced (as shown in **1a**). These clouds generate a different  $\text{Y}_2\text{O}_3$  content in the coated samples with respect to how close it was located with respect to the pure yttria ingot in the coating chamber. Therefore, the produced samples exhibited a  $\text{YO}_{1.5}$  content ( $\text{ZrO}_2$  balanced) in between 43 to 67  $\text{YO}_{1.5}$  mol %.

## 2.2 Infiltration Experiments

The selected CMAS source was natural volcanic ash (VA) collected from the Eyjafjallajökull volcano. Its composition is given by  $\text{C}_{11}\text{M}_6\text{A}_{13}\text{S}_{45}\text{F}_{16}\text{T}_4\text{L}_5$  where each letter represents every oxide in mol % using single cation basis ( $\text{CaO}$ ,  $\text{MgO}$ ,  $\text{AlO}_{1.5}$ ,  $\text{SiO}_2$ ,  $\text{FeO}$ ,  $\text{TiO}_2$  and L which represents the sum of  $\text{Na}_{0.5}\text{O}$  and  $\text{K}_{0.5}\text{O}$ ). Its composition was determined by energy dispersive X-Ray spectroscopy (EDS) using different powder samples. The estimated melting range of the Iceland VA is in between  $1060$  and  $1150 \text{ }^\circ\text{C}$ . It was measured via differential scanning calorimetry (DSC) in previous studies <sup>[30]</sup>. The volcanic ash infiltration experiments were performed by mixing the VA with distilled water. Subsequently, the slurry was

deposited on top of the coatings corresponding to an ash concentration of 20 mg/cm<sup>2</sup> and dried at ambient temperature for 2 h. The heat treatment was performed with a heating rate of about 80 K/min followed by isothermal treatment at 1250 °C for 1 h and subsequently cooled down (using extra fans) to room temperature at an average rate of 18 K/sec with a faster cooling rate at the beginning of cooling. The infiltrated samples were cut in half and prepared metallographically for microscopy inspection. Complementary experiments for 1 h isothermal infiltration were performed as well using a box furnace for slow furnace heating/cooling at 10K/min.

### ***2.3 Yttria-Zirconia Powder Preparation***

Yttria-zirconia powders in the compositions ranging from 50 to 80YO<sub>1.5</sub> were synthesized by co-deposition of stoichiometric aqueous solutions of ZrCl<sub>2</sub>\*8H<sub>2</sub>O and Y(NO<sub>3</sub>)<sub>3</sub>\*6H<sub>2</sub>O (Alfa Aesar, 99 %+ purity) on a hot plate at 400°C. The obtained composition products were crushed and subsequently heat treated at 1200 °C for 1 h in a chamber furnace. Additionally, pure Y<sub>2</sub>O<sub>3</sub> powders (Alfa Aesar 99.9 % purity) were also used to compare the pure YO<sub>1.5</sub>/Iceland VA XRD reactions.

## **2.4 Characterization**

### ***2.4.1 Microscopy Analysis***

Cross-sectional scanning electron microscope images (SEM) were obtained from the infiltrated samples to assess the VA infiltration damage. The infiltrated samples were covered with a epoxy (Gatan G2) and cut in half using a diamond saw automated machine. The cross-sections were then embedded in a conductive epoxy and polished down to a 0.05 µm finish using standard metallographic techniques. A DSM Ultra 55 (Carl Zeiss NTS, Wetzlar, Germany) SEM microscope equipped with an EDS system (Inca, Oxford Instruments

Abingdon, UK) was used to determine compositions of the crystalline phases and microstructural analysis. Focused ion beam (FIB) assisted transmission electron microscopy (TEM) was used to analyze the coatings after 1-hour infiltration from a non-infiltrated region. The used equipment were a Strata 205 FIB machine and a Tecnai F30 TEM-STEM utilizing a field-emission gun (FEI Inc., Eindhoven, Netherlands).

#### **2.4.2 XRD Studies**

Phase identification was done via X-ray diffraction (XRD) of synthesized yttria-zirconia powders mixed with Iceland VA. The process for yttria-zirconia powder synthesis is explained in the next section. The powder mixtures of 60 wt % of Iceland VA and 40 wt % of yttria-zirconia were ground in a mortar with ethanol until homogenization was achieved and heat treated via air rapid cooling as explained before for 10 hours on top of a Pt foil. Then, the heat-treated powder mixture was mechanically removed from the Pt foil and pulverized in a mortar to get a fine powder for XRD analysis. The XRD measurements were carried out using a Si single crystal holder and a Siemens D5000 diffractometer equipped with a  $\text{CuK}\alpha$  radiation source with a secondary graphite monochromator (EVA/Topas 4.2 software package, Bruker AXS, Karlsruhe, Germany). The XRD of the as coated samples was performed on samples still attached to the alumina substrate.

### **3. Results**

#### **3.1 Microstructure and Phase Analysis of TBCs and Synthesized $\text{YO}_{1.5}$ Powders**

The as-coated samples exhibited the typical parallel columnar structure generated by EB-PVD methods. **Figure 2** shows the microstructure for the as coated samples from the lowest  $\text{YO}_{1.5}$  (top left) and highest (bottom left) with the compositions of 43 and 67 mol%

(ZrO<sub>2</sub> balanced) respectively. The microstructure of both the samples exhibit parallel columnar growth with enlarged feather arms (2-5 μm long) compared to standard 7YSZ microstructures (0.5-3 μm) [37]. Both samples showed a 2 μm thick deposited layer of alumina (referred as AlO<sub>1.5</sub> in Fig. 2) with an approximated composition of 18.6AlO<sub>1.5</sub>, 25.4YO<sub>1.5</sub> and 56ZrO<sub>2</sub> in the low yttria side and 10.4AlO<sub>1.5</sub>, 50.8YO<sub>1.5</sub> and 38.8ZrO<sub>2</sub> in the high yttria side. The uniform alumina layer was a result of the involuntary short evaporation of one alumina substrate that fell into the molten evaporation pool due to the high rotations used during deposition. At this point it could not be ruled out that such a small amount of additional alumina alloyed in the coatings can influence the CMAS crystallization behavior. Therefore, the potential alumina effect is presented in detail in the discussion section.

The XRD patterns of as-deposited and as-synthesized YO<sub>1.5</sub>-ZrO<sub>2</sub> coatings and powders are shown in **Figure 3**. No significant peaks from the alumina-rich deposited layer are evident in the XRD patterns for the TBCs. This is expected since previous Al<sub>2</sub>O<sub>3</sub> EB-PVD experiments generally produced amorphous as-deposited alumina coatings [38]. The crystalline phase could be indexed as a cubic fluorite YSZ phase for the as-coated TBCs. In the case of as synthesized powders (**Figure 3b**), the fluorite lattice constant is increased with yttria additions until the 80YO<sub>1.5</sub> composition where the pure cubic yttria peaks start to appear. These small yttria peaks are slightly distinguished in the 67YO<sub>1.5</sub> TBC sample. It is difficult to extract conclusions of the produced phases in the as coated TBCs from the XRD analysis compared with the as synthesized powders since different material layers could possibly grow from the evaporation technique due to different vapor plume densities and beam fluctuations.

### 3.2 XRD Analysis of the CMAS/TBC Interaction

The reaction products produced during the annealing of VA/YO<sub>1.5</sub> powder mixtures were analyzed by XRD as shown in **Figure 4**. The XRD patterns indicate the apatite (A) and

garnet (G) phases as common reaction products among all the reactions involving yttria and VA (50YO<sub>1.5</sub> to pure YO<sub>1.5</sub>). The XRD peaks clearly indicate a trend, where the probability for apatite formation increases with respect to the yttria content in the coating i.e., availability of yttria as “solute” increases in the glass. This is due to the fact that most intense apatite peaks are observed for the pure YO<sub>1.5</sub> sample followed by the 80, 65 and 50 YO<sub>1.5</sub> samples, respectively. Apparently 50YO<sub>1.5</sub> is the limit to promote apatite formation, as observed in the present study. The garnet formation seems to be un-affected regardless of the YO<sub>1.5</sub> content in the reaction. Garnet also appears to be the silicate-based phase with the highest concentration (highest peak formation) in the reaction. As expected, the fluorite phase (F) was found for all powder mixtures containing ZrO<sub>2</sub> (80 to 50 YO<sub>1.5</sub>) since it is the dominant host phase for ZrO<sub>2</sub>. It is also known that the ZrO<sub>2</sub> solubility in the glass is lower than that of the YO<sub>1.5</sub> [39]. This promotes the nucleation of ZrO<sub>2</sub> bearing crystals which capture YO<sub>1.5</sub> to crystalize as any of the three available YSZ phases (monoclinic, tetragonal or cubic fluorite) depending on the composition of the melt [39-42]. A zirconolite-type phase ‘Z’ (Zirconolite: nominally CaZrTi<sub>2</sub>O<sub>7</sub>) was identified for all the ZrO<sub>2</sub> bearing mixtures only. A summary of the identified reaction products and their theoretical chemical formulae is presented in **Table 1**. The Z and F phases can accommodate Y<sup>3+</sup>, this reduces the amount of Y<sup>3+</sup> available to promote apatite formation. Finally, it is important to note that all the pure YO<sub>1.5</sub> powder was consumed in the crystallization reaction since no traces of the cubic yttria phase (peak) are visible after the heat treatment test.

### 3.3 Volcanic Ash Melt Infiltration

**Figure 5** shows the cross-sectional image of the Iceland VA infiltrated samples with 4 different YO<sub>1.5</sub> average compositions of the TBC (43, 53, 60 and 67 mol%, respectively) after 1 h at 1250 °C followed by rapid cooling. The reaction phases were identified similar to the XRD studies (apatite, garnet, fluorite and zirconolite) with help of the composition

measurements using EDS and co-relating with the XRD found phases and literature. It is clearly seen that 43YO<sub>1.5</sub> sample (**Figure 5a**) has undergone some reaction with the VA; however, no apatite formation (A) was found in the layer. At the reaction front a uniform zirconolite (Z) layer is visible on top of the TBC/glass interface with a thickness of 1-2 μm. Large globular fluorite crystals (F) are seen distributed evenly throughout the reaction layer (delimited within the dotted lines in the other figures). Lastly, no garnet phase (G) presence is identified in 43YO<sub>1.5</sub>. In contrast, the 53 to 67 YO<sub>1.5</sub> reactions exhibit different reaction products than that of 43YO<sub>1.5</sub>. Apatite crystals (A) are clearly seen in small confined areas such as small columnar gaps or feather arms and they clearly grow favorably to seal the gaps and their presence becomes more prominent with the higher yttria content.

The garnet phase appears to be engulfing the other products at the glass/TBC interphase (apatite, garnet and zirconolite) but it seems to consume mainly the apatite phase in the columnar gaps (see Fig. **5d**). This type of growth is in agreement with the hypothesis that the garnet phase represents a secondary reaction product, which grows or nucleates slower at expense of other phases from the constant interaction with the glass <sup>[43]</sup>. Fluorite and zirconolite phases are clearly distinguished in all the reactions; however, the amount of fluorite decreases and partly appears to transform into zirconolite with increasing yttria content. The 53YO<sub>1.5</sub> emerges to be the compositional threshold for the apatite. These results are in agreement with the XRD studies discussed earlier. The reaction zone gets thinner with respect to the increase in YO<sub>1.5</sub> content: 23, 20 and 18 μm for the 53, 60 and 67 YO<sub>1.5</sub> respectively.

The coating containing YO<sub>1.5</sub> from 47 to 60 percent exhibited full infiltration of the 50 μm thick top coat having an additional reaction at the underneath 67YO<sub>1.5</sub> layer. The 67YO<sub>1.5</sub> top layer was the only one that did not show complete infiltration as seen from **Figure 6** where the Si and Ca elemental maps (given in green and pink colors respectively) show the

localized infiltration at large columnar gaps at about 40  $\mu\text{m}$  maximum. The elemental mapping shows a clear Ti enrichment in the zirconolite layer. This phase was seen in previous experiments at 1250  $^{\circ}\text{C}$  at various heat treatment durations (5 min to 20 h) <sup>[30]</sup> but it was finally identified in this study. Additionally, the zirconolite phase was also found after long heat treatments (100 h) for  $\text{Gd}_2\text{Zr}_2\text{O}_7$  TBCs tested with an artificial volcanic ash produced matching the composition of the Iceland VA collected from a different ash plume event <sup>[34]</sup>. This phase is believed to be closely related to the pyrochlore structure and is also structurally related to the zirkelite and polymignyte minerals <sup>[44-46]</sup>. The garnet phase showed a characteristic Fe enrichment as seen in **Figure 6**. These findings are consistent with previous studies with Iceland VA <sup>[30]</sup>.

#### **4. Discussion**

The results obtained on as-deposited and reacted samples and their reaction products are discussed to understand the performance of the proposed TBCs in CMAS infiltration experiments. The effect of composition and microstructure along with the reaction kinetics can be understood from the results obtained in the experiments performed using Iceland VA as CMAS bearing source in interaction with TBCs produced by jumping beam evaporation with varying  $\text{YO}_{1.5}$  content at 1250  $^{\circ}\text{C}$ . Results and their implications on the infiltration performance are discussed in the following section.

##### **4.1 Effects of Deposited Alumina in the Reaction with VA**

The presence of  $\text{AlO}_{1.5}$  in the 2  $\mu\text{m}$  thick top layers of the yttria-zirconia, which was accidentally deposited on top of the intended yttria rich layers, was found to be amorphous in nature. As stated before, previous studies using EB-PVD alumina coatings were amorphous after the deposition and additional heat treatments were needed to stabilize the  $\alpha$  alumina phase <sup>[38]</sup>. The estimated amount of dissolved alumina from the coating would be very minimal which could count about 0.4 vol % of the CMAS deposit (estimated by the average

deposited CMAS volume on top the TBC (about  $3.51 \text{ mm}^3$ ) and the alumina volume content in the  $2 \text{ }\mu\text{m}$  thick alumina bearing layer ( $0.015 \text{ mm}^3$ ). These amounts are essentially negligible for the VA melt equilibrium. However, this alumina could lead to the formation of alumina-yttria based phases such as YAG ( $\text{Y}_3\text{Al}_5\text{O}_{12}$ ), YAP ( $\text{YAlO}_3$ ) and YAM ( $\text{Y}_4\text{Al}_2\text{O}_9$ ) upon heat treatment <sup>[47, 48]</sup>. Special interest has been paid to these phases since they have exhibited potential as a CMAS resistant coating <sup>[49, 50]</sup>. Since the alumina and zirconia are not expected to form any crystalline phase <sup>[51]</sup>, only attention was paid to the Al-Y mixture. In this context, TEM studies were performed on the 1 h heat treated sample at  $1250 \text{ }^\circ\text{C}$  in the non-VA infiltrated region to look for possible Y-Al phases. The TEM results are shown in **Figure 7** for the top alumina mix layer in the  $67\text{YO}_{1.5}$  sample. The results indicate nonmixing of the alumina and zirconia as expected but it also showed no mixed yttria-alumina phases. The Al was found to be located in small polycrystalline inclusions, presumably as a  $\gamma\text{-Al}_2\text{O}_3$  phase. Additionally, cubic fluorite YSZ crystals were found in this region. Furthermore, the TEM results in the column core are also shown. The base material at the column core had a lanthanide cubic type yttria structure with alternating layers of fully stabilized cubic fluorite YSZ phase of varying content. This is due to the jumping beam evaporation process which produces an intermixing layer which is the function of the jumping beam frequency <sup>[52]</sup>. Thus, it can be concluded that no reaction products are formed from the alumina additions into the coating, as well as negligible effects of the alumina dissolution into the molten glass to promote different reaction phase formation.

#### **4.2 Effects of Y contents in the Interactions with VA and Reaction Phase Formation**

Having addressed the uniqueness of the TBC composition, we now turn our attention to the effect of reaction phase formation with  $\text{YO}_{1.5}$  content. It is well known that the most desirable phase for CMAS resistance is the apatite since it represents the first and fastest

silicate based phase to crystallize upon yttria saturation in the glass <sup>[11, 31]</sup>. Additionally, its crystallization morphology/configuration within the columnar gaps allow sealing them effectively; therefore, no more glass is allowed to infiltrate through the columnar gaps. This crystallization behavior is believed to be beneficial in the initial infiltration stages (first few minutes of interaction) for porous TBC microstructures. However, it is suggested that after long-term heat treatment (more than 1 h) it is important that the coating consumption rate (or reaction layer growth) is minimum so the need of thick sacrificial coatings is reduced. Additionally, since the reported CMAS glasses and VAs exhibit a large variety of oxides such as Fe, Ti, K and Na, it is important that the reaction phases are able to retain more glass and more oxides per consumed TBC amount (i.e. Y and Zr). In this context, the garnet phase appears to be the most beneficial phase at the long-term infiltration since compared to the other phases it retains less TBC material i.e., glass g/TBC is highest as seen in **Figure 8**. The determination of this ratio is based on the mole percentage of glass products “g” (Ca, Al, Mg, Si, Fe, Ti) with respect to the mole percentage of coating material “TBC.” Furthermore, studies performed comparing a vigorous apatite former TBC material such as  $Gd_2Zr_2O_7$  (referred as GZO) have shown a larger reaction layer growth for the GZO. These results support the hypothesis that the garnet phase appears to be beneficial for the long-term infiltration. The composition summary for the reaction products formed on the reaction layer for the  $67YO_{1.5}$  coating after 1 h at 1250 °C is shown in **Table 2** for the experiments performed.

The importance of the early and quick formation of apatite phase was discussed above. Therefore, the present work and the results obtained demonstrate that, in order to have a CMAS/VA resistant  $YO_{1.5}$  based coating, a minimum amount of  $50YO_{1.5}$  (shown in the XRD and TBC results) is required to promote the formation of this apatite phase. The thinner reaction layer with respect to higher yttria content in the coating leads to the conclusion that

more yttria available for reaction is needed to generate more apatite (consuming less coating material to crystallize the melt), which is also supported by the XRD results. This can be explained from the phase equilibria of pure yttria and yttria-zirconia coatings seen in the  $Y_2O_3$ - $ZrO_2$  phase diagram shown in **Figure 9**, which is adapted from [53-55]. The red dashed line in Fig. 9 indicates the testing temperature of 1250 °C. As the coating material is dissolved by the glass the  $Zr^{4+}$  re-precipitates upon reaching a saturation limit (about two times less than  $Y^{3+}$ ) [39]. Since the glass is enriched in  $Y^{3+}$  as well, the fluorite phase is promoted which can retain about 16  $YO_{1.5}$  percent minimum at 1250 °C. From this point the  $Y^{3+}$  ion partitions into fluorite and apatite formation. From the XRD results, the 80 $YO_{1.5}$  powder sample represented the sample with the maximum  $YO_{1.5}/ZrO_2$  ratio tested, as seen from the phase diagram this leaves more  $Y^{3+}$  ions available to divide into apatite and fluorite. However, since the Zr content is reduced for higher  $YO_{1.5}$  contents less fluorite phase can be promoted which provides more free yttria available for reaction in the system. From this analysis it is then expected that the pure free  $YO_{1.5}$  composition will maximize apatite formation since the cubic fluorite will not be present. It has been proposed that fluorite formation limits apatite formation for RE compositions and this reaction changes with respect of RE ionic radius [43, 56], this is due to the change in fluorite phase stability depending on the doped RE. The current results show that the limited amount of available yttria for reaction to promote apatite is constrained to the point where the pure fluorite phase (F) starts to form; this is in good agreement with the literature reports. Additionally, we report that the compositional limit to promote glass reaction is with 50 $YO_{1.5}$  compositions as confirmed from the TBC and XRD experiments. Thus, it is evident that below this 50 $YO_{1.5}$  amount there is not enough free yttria available to promote apatite formation from its dissolution into the glass. Therefore, the apatite cannot precipitate as seen for the 43 $YO_{1.5}$  composition. Similar results were found in experiments performed with Yb-Hf based pellets with similar

phase fields as for the  $\text{YO}_{1.5}\text{-ZrO}_2$  (e.g. fluorite and  $\delta$  phase) performed by Poerschke et al. [23]. In their studies apatite formation was promoted for the  $\delta$  Yb-Hf phase ( $56\text{YbO}_{1.5}$  composition) but it was not promoted for the  $30\text{YbO}_{1.5}$  tested composition. The study concluded that the low Yb composition did not form apatite since the dissolved Yb was retained in the fluorite phase or in solution in the melt and as more Yb was added the system could saturate in Yb to promote apatite formation. It is important to note that the boundary for formation of the  $\delta$  phase ( $\text{Zr}_3\text{Y}_4\text{O}_{12}$ ) still allows the apatite formation as found in the literature [11, 56] since it exhibits a  $57\text{YO}_{1.5}$  content which still has potential to give out excess yttria for dissolution prior fluorite formation. One more hypothesis can be drawn from the phase diagram. It is seen at higher temperatures (e.g.  $1400\text{ }^\circ\text{C}$ ) that the fluorite phase field expands into wider yttria compositions of about 14 mol %  $\text{YO}_{1.5}$  at the lowest and 61 % at the highest. This range is seen to expand even further with increasing temperatures. This leads to the conclusion that the potency of apatite formation for yttria rich-zirconia coatings at temperatures above  $1300\text{ }^\circ\text{C}$  will be reduced due to the thermodynamic preference to promote fluorite nucleation with lesser yttria contents which reduces more the yttria available for reaction. In contrast, the pure yttria would promote pure apatite crystallization since it would not produce any fluorite formation upon  $\text{Y}^{3+}$  dissolution (since no  $\text{Zr}^{4+}$  is available in the reaction) which theoretically would make a better candidate for CMAS/VA infiltration resistance. On the contrary, experiments performed by Eils et al. [31] using pure yttria and  $\text{Y}_2\text{O}_3\text{-ZrO}_2$  coatings showed lower CMAS infiltration for the  $\text{Y}_2\text{O}_3\text{-ZrO}_2$  coating than the pure yttria coating. However, the microstructure of both coatings was not analyzed (not providing data for permeability of each coating) which makes it difficult to draw any conclusions from these results. It is important to stress that also that microstructure plays a prominent role in CMAS infiltration. For instance, for EB-PVD coatings, the microstructure can be tailored to reduce CMAS infiltration by effectively distributing the flow of the molten glass [36, 57]. Also,

very wide columnar gaps may allow large volumes of glass to infiltrate first/before apatite formation starts which could shift the saturation limit of the melt retarding the apatite formation. Therefore, a comprehensive study of microstructural infiltration effects is needed to effectively evaluate the infiltration resistance for coatings with different compositions.

It must be emphasized that our motivation to use yttria-zirconia based coatings comes from some limitations that pure yttria exhibits such as low toughness compared to fluorite YSZ<sup>[58]</sup> and higher thermal conductivity<sup>[59]</sup>. It is reported that the increase in yttria in the fluorite lowers the thermal conductivity<sup>[59, 60]</sup> up to 32YO<sub>1.5</sub>, after that the thermal conductivity starts to increase again<sup>[61]</sup>. The performed CMAS experiments show the superior protective behavior of the highest yttria bearing coating (67YO<sub>1.5</sub> or about 65 wt % Y<sub>2</sub>O<sub>3</sub>).

Finally, the zirconolite phase appears to nucleate from the Y-Zr dissolution in the Ti-rich glass. A similar Zr-Ti bearing phase identified as calzirtite (Ca<sub>2</sub>Zr<sub>5</sub>Ti<sub>2</sub>O<sub>16</sub>) with a diffraction match with zirconolite was identified by Vidal-Setif et al.<sup>[62]</sup> in high pressure turbine blades removed from military airplane engines under CMAS attack. This phase has also been reported with gadolinium zirconate interaction with artificial volcanic ashes bearing Ti<sup>[34]</sup>. It exhibits a general stoichiometry of A<sub>2</sub>B<sub>2</sub>X<sub>7</sub> where A= Ca, Na, RE, Zr, Ti and actinoids (ACT). B= Ti, Nb, Ta, Al, Mg and Fe and X= O or F<sup>[44, 45, 63, 64]</sup>. It is seen that a wide variety of elements can be accommodated in solid solution but the main constituents appear to be Zr and Ti<sup>[45]</sup>. It is believed that trivalent Ti<sup>3+</sup> can be incorporated in the A site in small amounts<sup>[65]</sup> but due to the large content of available cations in these experiments and no evidence for the presence of Ti<sup>3+</sup>, it is assumed that Ti exclusively occupies the B site as Ti<sup>4+</sup>. Additionally, no reports in literature were found about the possible incorporation of Si. It is important to note that the zirconolite phase requires less yttria compared to apatite since it was formed already in the 43YO<sub>1.5</sub> TBC sample. Additionally, it retains a significant

amount of  $Y^{3+}$  (up to 23 mol% as seen from **Table 2**) which could be problematic since it represents an additional sink for  $Y^{3+}$  which cannot be used for apatite formation. Conversely, this phase was only found in the upper reaction layer only in interaction with the glass reservoir and not in the columnar gaps. This could mean that a special precipitation mechanism is required for this phase where an interaction with large glass contents is required. Additionally, this phase has been found to be present in the reaction layer up to 50 h at 1250 °C with yttria based TBC interactions (67YO<sub>1.5</sub> yttria contents) and also in GZO reactions up to 100 h at 1200 °C<sup>[34]</sup>. These results show how dynamically complex these reactions are and the strong influence in the phase equilibria that other cations such as Ti have. Therefore, a comprehensive understanding on the thermodynamic influence that different cations have in the system could significantly help in predicting the CMAS/VA infiltration resistance of TBCs.

#### **4.3 Effects of Varying Cooling Rates in Reaction Product Formation**

Finally, we now turn our attention to the effect of cooling rate on the crystallization of the reaction products and the implications. Note that the aircraft engines are subjected to very abrupt temperature changes during operation e.g., take-off, cruise and landing <sup>[66]</sup>. The landing stage is very critical since it produces a very severe temperature drop in the material from the reverse thrust to the ground idle stages. This makes the use of air quenched experiments discussed above a more approximate testing condition for the actual engine operating cycle. Besides, by using this testing approach, the high temperature phases are retained so they can be analyzed. In order to investigate if there is any phase nucleation upon cooling, the CMAS infiltration experiments were performed one more time under slow heating and cooling (10K/min) conditions using a box furnace. The reaction layers after the heat treatments are shown in **Figure 10** for the 43 and 67YO<sub>1.5</sub> TBCs only. The reaction products, consisting of A, G, F, etc., were found but an additional phase consisting of

dendritic particles (d) in the molten glass zone was distinguished compared to the air quenched samples. These dendrites were also found for the Iceland VA in previous tests with slow furnace cooling and they exhibited all available cations in their composition <sup>[30]</sup>. These particles retained all possible cations (Fe, Ca, Y, Zr, etc.) in them and were identified as garnet dendrites but they exhibited a larger Fe content (21.3 mol %); the cation-only composition being approximately  $\text{Mg}_{9.9}\text{Al}_{9.9}\text{Si}_{29.5}\text{Ca}_{11}\text{Ti}_{1.2}\text{Fe}_{21.3}\text{Y}_{17.3}$ . Thus, the current experiments proved that the nucleation of these particles is driven by the slow diffusion control growth from the slow cooling rate of 10 K/min. Additionally, very small dendrites were also found in the air quenched samples with sizes below 1  $\mu\text{m}$  (**Figure 10c**). However, their presence in the air quenched samples was not as dominant as in the slow cooled TBC samples which supports the findings on their diffusion enhanced growth due to the slow cooling process.

Furthermore, the infiltration depth exhibited for the slow cooled samples was practically the same as for the air quenched samples. A clear formation of garnet crystals is seen in the  $43\text{YO}_{1.5}$  TBC sample (**Figure 10a**) which were not seen in its counterpart under air quenched conditions (**Figure 5a**). Additionally, the garnet crystals appear to be nucleating at the expense of the fluorite globular particles in the slow cooling case. Also, higher conglomeration and larger garnet crystals are seen for all the slow cooled TBC samples. These findings are in agreement with the reported garnet growth behavior in literature which is enhanced during slow cooling and by the consumption of apatite and fluorite phases <sup>[11]</sup>.

## 5 Conclusions

Experiments were performed using Iceland VA as CMAS bearing source in interaction with TBCs produced by jumping electron-beam physical vapor deposition with varying  $\text{YO}_{1.5}$  content at 1250 °C. The infiltration resistance of the coatings was assessed with respect to the  $\text{YO}_{1.5}$  content in the coating and supplemental studies with VA/ $\text{YO}_{1.5}$

synthesized powder mixtures were performed for phase identification. The results have given the following conclusions:

- The results from XRD powder mixtures and TBC coating experiments showed that higher VA infiltration resistance is expected with higher  $YO_{1.5}$  as solute to promote apatite formation in order to seal the columnar gaps. Thinner reaction layer is also expected with higher yttria contents.
- The reaction showed that 50 $YO_{1.5}$  contents in the coating appears to be the lower compositional limit to promote apatite formation as reaction product. This phase reaction exhibits a correlation with the fluorite phase formation and free yttria available for reaction which is also a function of infiltration temperature.
- The growth of the garnet phase is enhanced due to the diffusion-controlled growth mechanism produced during slow cooling. Additionally, the garnet dendrite phase also exhibited the same slow diffusion-controlled growth process. Their compositions did not vary significantly with respect of heat treatment.
- The high Ti contents in the glass promote the zirconolite phase formation which accommodated large amounts of  $Y^{3+}$  and nucleates with lower yttria contents in the coating (43 $YO_{1.5}$ ) compared to apatite. This shows the urgency to understand the effects of other cations within CMAS for the phase equilibria to effectively predict phase formation and to guide the development of more CMAS-recession tolerant TBCs.

## **Acknowledgements**

The authors thank D. Peters and J. Brien for their assistance in producing the EB-PVD samples. Special thanks to A. Handwerk for his technical assistance in experimental testing. The authors express their gratitude to P. Bauer and F. Kerpps for their assistance with FIB sample preparation. The authors thank the following funding agencies for providing partial funding for this project implementation: The Deutsche Forschungsgemeinschaft (DFG) under grant Schu1372/5-1, Consejo Nacional de Ciencia y Tecnologia (CONACYT) and National Science Foundation (NSF) with NSF-PREM grant no. DMR-1827745.

## References

1. Padture, N.P., M. Gell, and E.H. Jordan, *Thermal Barrier Coatings for Gas Turbine Engine Applications*. Science, 2002. **296**: p. 280-284.
2. Padture, N.P., *Advanced structural ceramics in aerospace propulsion*. Nature Materials, 2016. **15**: p. 804-809.
3. Clarke, D.R., M. Oechsner, and N.P. Padture, *Thermal-barrier coatings for more efficient gas-turbine engines*. MRS Bulletin, 2012. **37**: p. 891-898.
4. Evans, A.G., D.R. Clarke, and C.G. Levi, *The influence of oxides on the performance of advanced gas turbines*. Journal of the European Ceramic Society, 2008. **28**: p. 1405-1419.
5. Darolia, R., *Thermal barrier coatings technology: critical review, progress update, remaining challenges and prospects*. International Materials Reviews, 2013. **58**: p. 315-348.
6. Schulz, U., et al., *Review on Advanced EB-PVD Ceramic Topcoats for TBC Applications*. International Journal of Applied Ceramic Technology, 2005. **1**: p. 302-315.
7. Clarke, D.R. and S.R. Phillpot, *Thermal barrier coating materials*. Materials Today, 2005. **8**(6): p. 22-29.
8. Levi, C.G., *Emerging materials and processes for thermal barrier systems*. Current Opinion in Solid State and Materials Science, 2004. **8**: p. 77-91.
9. Sampath, S., et al., *Processing science of advanced thermal-barrier systems*. MRS bulletin, 2012. **37**: p. 903-910.
10. Levi, C.G., et al., *Environmental degradation of thermal-barrier coatings by molten deposits*. MRS Bulletin, 2012. **37**: p. 932-941.
11. Poerschke, D.L., R.W. Jackson, and C.G. Levi, *Silicate Deposit Degradation of Engineered Coatings in Gas Turbines: Progress Toward Models and Materials Solutions*. Annual Review of Materials Research, 2017. **47**(1): p. 297-330.
12. Grant, K.M., et al., *CMAS degradation of environmental barrier coatings*. Surface and Coatings Technology, 2007. **202**: p. 653-657.
13. Grant, K.M., et al., *Calcium–Magnesium Alumino-Silicate Interaction with Yttrium Monosilicate Environmental Barrier Coatings*. Journal of the American Ceramic Society, 2010. **93**: p. 3504-3511.
14. Harder, B.J., et al., *Chemical and mechanical consequences of environmental barrier coating exposure to calcium–magnesium–aluminosilicate*. Journal of the American Ceramic Society, 2011. **94**.
15. Poerschke, D.L., et al., *Interaction of yttrium disilicate environmental barrier coatings with calcium-magnesium-iron alumino-silicate melts*. Acta Materialia, 2018. **145**: p. 451-461.
16. Summers, W.D., et al., *Roles of composition and temperature in silicate deposit-induced recession of yttrium disilicate*. Acta Materialia, 2018. **160**: p. 34-46.
17. Mercer, C., et al., *A delamination mechanism for thermal barrier coatings subject to calcium-magnesium-alumino-silicate (CMAS) infiltration*. Acta Materialia, 2005. **53**: p. 1029-1039.
18. Li, G., et al., *Zirconium silicate growth induced by the thermochemical interaction of yttria-stabilized zirconia coatings with molten CMAS deposits*. Corrosion Science, 2019. **149**: p. 249-256.

19. Zhu, W., et al., *The evolution of pores in thermal barrier coatings under volcanic ash corrosion using X-ray computed tomography*. *Surface and Coatings Technology*, 2019. **357**: p. 372-378.
20. Yang, L., et al., *Acoustic emission monitoring and damage mode discrimination of APS thermal barrier coatings under high temperature CMAS corrosion*. *Surface and Coatings Technology*, 2016. **304**: p. 272-282.
21. Clarkson, R.J., E.J.E. Majewicz, and P. Mack, *A re-evaluation of the 2010 quantitative understanding of the effects volcanic ash has on gas turbine engines*. *Proceedings of the Institution of Mechanical Engineers, Part G: Journal of Aerospace Engineering*, 2016. **230**(12): p. 2274-2291.
22. Poerschke, D.L., et al., *Stability and CMAS Resistance of Ytterbium-Silicate/Hafnate EBCs/TBC for SiC Composites*. *Journal of the American Ceramic Society*, 2015. **98**(1): p. 278-286.
23. Poerschke, D.L., G.G.E. Seward, and C.G. Levi, *Influence of Yb:Hf Ratio on Ytterbium Hafnate/Molten Silicate (CMAS) Reactivity*. *Journal of the American Ceramic Society*, 2016. **99**(2): p. 651-659.
24. Drexler, J.M., et al., *Plasma sprayed gadolinium zirconate thermal barrier coatings that are resistant to damage by molten Ca-Mg-Al-silicate glass*. *Surface and Coatings Technology*, 2012. **206**: p. 3911-3916.
25. Drexler, J.M., et al., *Jet engine coatings for resisting volcanic ash damage*. *Advanced Materials*, 2011. **23**: p. 2419-2424.
26. Gledhill, A.D., et al., *Mitigation of damage from molten fly ash to air-plasma-sprayed thermal barrier coatings*. *Materials Science and Engineering: A*, 2011. **528**: p. 7214-7221.
27. Krause, A.R., et al., *Resistance of 2ZrO<sub>2</sub>-Y<sub>2</sub>O<sub>3</sub> top coat in thermal/environmental barrier coatings to calcia-magnesia-aluminosilicate attack at 1500°C*. *Journal of the American Ceramic Society*, 2017. **100**(7): p. 3175-3187.
28. Krause, A.R., et al., *2ZrO<sub>2</sub>-Y<sub>2</sub>O<sub>3</sub> thermal barrier coatings resistant to degradation by molten CMAS: Part II, Interactions with sand and fly ash*. *Journal of the American Ceramic Society*, 2014. **97**: p. 3950-3957.
29. Krause, A.R., et al., *2ZrO<sub>2</sub>-Y<sub>2</sub>O<sub>3</sub> thermal barrier coatings resistant to degradation by molten CMAS: Part I, Optical basicity considerations and processing*. *Journal of the American Ceramic Society*, 2014. **97**: p. 3943-3949.
30. Naraparaju, R., et al., *Interaction and infiltration behavior of Eyjafjallajökull, Sakurajima volcanic ashes and a synthetic CMAS containing FeO with/in EB-PVD ZrO<sub>2</sub>-65 wt% Y<sub>2</sub>O<sub>3</sub> coating at high temperature*. *Acta Materialia*, 2017. **136**: p. 164-180.
31. Eils, N.K., P. Mechnich, and W. Braue, *Effect of CMAS Deposits on MOCVD Coatings in the System Y<sub>2</sub>O<sub>3</sub>-ZrO<sub>2</sub>: Phase Relationships*. *Journal of the American Ceramic Society*, 2013. **96**: p. 3333-3340.
32. Schulz, U. and W. Braue, *Degradation of La<sub>2</sub>Zr<sub>2</sub>O<sub>7</sub> and other novel EB-PVD thermal barrier coatings by CMAS (CaO-MgO-Al<sub>2</sub>O<sub>3</sub>-SiO<sub>2</sub>) and volcanic ash deposits*. *Surface and Coatings Technology*, 2013. **235**: p. 165-173.
33. Krämer, S., J. Yang, and C.G. Levi, *Infiltration-inhibiting reaction of gadolinium zirconate thermal barrier coatings with CMAS melts*. *Journal of the American Ceramic Society*, 2008. **91**: p. 576-583.
34. Mechnich, P. and W. Braue, *Volcanic ash-induced decomposition of EB-PVD Gd<sub>2</sub>Zr<sub>2</sub>O<sub>7</sub> thermal barrier coatings to Gd-oxyapatite, zircon, and Gd, Fe-zirconolite*. *Journal of the American Ceramic Society*, 2013. **96**: p. 1958-1965.

35. Xia, J., et al., *On the resistance of rare earth oxide-doped YSZ to high temperature volcanic ash attack*. *Surface and Coatings Technology*, 2016. **307**: p. 534-541.
36. Naraparaju, R., et al., *Tailoring the EB-PVD columnar microstructure to mitigate the infiltration of CMAS in 7YSZ thermal barrier coatings*. *Journal of the European Ceramic Society*, 2017. **37**: p. 261-270.
37. Renteria, A.F., et al., *Effect of morphology on thermal conductivity of EB-PVD PYSZ TBCs*. *Surface and Coatings Technology*, 2006. **201**: p. 2611-2620.
38. Naraparaju, R., et al., *EB-PVD alumina (Al<sub>2</sub>O<sub>3</sub>) as a top coat on 7YSZ TBCs against CMAS/VA infiltration: Deposition and reaction mechanisms*. *Journal of the European Ceramic Society*, 2018. **38**(9): p. 3333-3346.
39. Krause, A.R., X. Li, and N.P. Padture, *Interaction between ceramic powder and molten calcia-magnesia-alumino-silicate (CMAS) glass, and its implication on CMAS-resistant thermal barrier coatings*. *Scripta Materialia*, 2016. **112**: p. 118-122.
40. Krämer, S., et al., *Thermochemical interaction of thermal barrier coatings with molten CaO-MgO-Al<sub>2</sub>O<sub>3</sub>-SiO<sub>2</sub> (CMAS) deposits*. *Journal of the American Ceramic Society*, 2006. **89**: p. 3167-3175.
41. Mechnich, P., W. Braue, and U. Schulz, *High-temperature corrosion of EB-PVD yttria partially stabilized zirconia thermal barrier coatings with an artificial volcanic ash overlay*. *Journal of the American Ceramic Society*, 2011. **94**: p. 925-931.
42. Krause, A.R., et al., *Calcia-magnesia-alumino-silicate (CMAS)-induced degradation and failure of air plasma sprayed yttria-stabilized zirconia thermal barrier coatings*. *Acta Materialia*, 2016. **105**: p. 355-366.
43. Poerschke, D.L. and C.G. Levi, *Effects of cation substitution and temperature on the interaction between thermal barrier oxides and molten CMAS*. *Journal of the European Ceramic Society*, 2015. **35**(2): p. 681-691.
44. White, T.J., *The microstructure and microchemistry of synthetic zirconolite, zirkelite and related phases*. *American Mineralogist*, 1984. **69**: p. 1156-1172.
45. Rossell, H.J., *Solid solution of metal oxides in the zirconolite phase CaZrTi<sub>2</sub>O<sub>7</sub>. I. Heterotype solid solutions*. *Journal of Solid State Chemistry*, 1992. **99**: p. 38-51.
46. Ringwood, A.E., et al., *Immobilisation of high level nuclear reactor wastes in SYNROC*. *Nature*, 1979. **278**: p. 219-223.
47. Medraj, M., et al., *High temperature neutron diffraction study of the Al<sub>2</sub>O<sub>3</sub>-Y<sub>2</sub>O<sub>3</sub> system*. *Journal of the European Ceramic Society*, 2006. **26**(16): p. 3515-3524.
48. Yin, B., et al., *Effect of Al<sub>2</sub>O<sub>3</sub> modification on the properties of YSZ: Corrosion resistant, wetting and thermal-mechanical properties*. *Surface and Coatings Technology*, 2019. **357**: p. 161-171.
49. Turcer, L.R., et al., *Environmental-barrier coating ceramics for resistance against attack by molten calcia-magnesia-aluminosilicate (CMAS) glass: Part I, YAlO<sub>3</sub> and  $\gamma$ -Y<sub>2</sub>Si<sub>2</sub>O<sub>7</sub>*. *Journal of the European Ceramic Society*, 2018.
50. Gell, M., et al., *Higher Temperature Thermal Barrier Coatings with the Combined Use of Yttrium Aluminum Garnet and the Solution Precursor Plasma Spray Process*. *Journal of Thermal Spray Technology*, 2018. **27**(4): p. 543-555.
51. Tarasi, F., et al., *Amorphous and crystalline phase formation during suspension plasma spraying of the alumina-zirconia composite*. *Journal of the European Ceramic Society*, 2011. **31**(15): p. 2903-2913.
52. Schulz, U., K. Fritscher, and C. Leyens, *Two-source jumping beam evaporation for advanced EB-PVD TBC systems*. *Surface and Coatings Technology*, 2000. **133-134**: p. 40-48.

53. Andrievskaya, E.R., *Phase equilibria in the refractory oxide systems of zirconia, hafnia and yttria with rare-earth oxides*. Journal of the European Ceramic Society, 2008. **28**(12): p. 2363-2388.
54. TRUBELJA, M.F. and V.S. STUBICAN, *Phase Equilibria and Ordering in the System Zirconia-Hafnia-Yttria*. Journal of the American Ceramic Society, 1988. **71**(8): p. 662-666.
55. Fabrichnaya, O., et al., *Phase equilibria and thermodynamic properties of the ZrO<sub>2</sub>-GdO<sub>1.5</sub>-YO<sub>1.5</sub> system*. Journal of Phase Equilibria and Diffusion, 2005. **26**(6): p. 591-604.
56. Poerschke, D.L., T.L. Barth, and C.G. Levi, *Equilibrium relationships between thermal barrier oxides and silicate melts*. Acta Materialia, 2016. **120**: p. 302-314.
57. Naraparaju, R., et al., *Estimation of CMAS Infiltration depth in EB-PVD TBCs: A new constraint model supported with experimental approach*. Journal of the European Ceramic Society, 2019.
58. Fantozzi, G., et al., *Effect of nonstoichiometry on fracture toughness and hardness of yttrium oxide ceramics*. Journal of the American Ceramic Society, 1989. **72**: p. 1562-1563.
59. Nicholls, J.R., et al., *Methods to reduce the thermal conductivity of EB-PVD TBCs*. Surface and Coatings Technology, 2002. **151-152**: p. 383-391.
60. Mévrel, R., et al., *Thermal diffusivity and conductivity of Zr<sub>1-x</sub>Y<sub>x</sub>O<sub>2-x/2</sub> (x=0, 0.084 and 0.179) single crystals*. Journal of the European Ceramic Society, 2004. **24**: p. 3081-3089.
61. Bisson, J.-F., et al., *Thermal Conductivity of Yttria-Zirconia Single Crystals, Determined with Spatially Resolved Infrared Thermography*. Journal of the American Ceramic Society, 2004. **83**: p. 1993-1998.
62. Vidal-Setif, M.H., et al., *Calcium-magnesium-alumino-silicate (CMAS) degradation of EB-PVD thermal barrier coatings: Characterization of CMAS damage on ex-service high pressure blade TBCs*. Surface and Coatings Technology, 2012. **208**: p. 39-45.
63. DELLA VENTURA, G., F. BELLATRECCIA, and C.T. WILLIAMS, *ZIRCONOLITE WITH SIGNIFICANT REEZrNb (Mn, Fe) O<sub>7</sub> FROM A XENOLITH OF THE LAACHER SEE ERUPTIVE CENTER, EIFEL VOLCANIC REGION, GERMANY*. The Canadian Mineralogist, 2000. **38**: p. 57-65.
64. Stefanovsky, S.V., et al., *XRD, SEM and TEM Study of the Gd-Doped Zirconolites*. MRS Online Proceedings Library Archive, 2002. **713**.
65. Bayliss, P., et al., *Mineral nomenclature: zirconolite*. Mineral. Mag, 1989. **53**: p. 565-569.
66. Reed, R.C., *The Superalloys fundamentals and applications*. The Superalloys: Fundamentals and Applications, 2006. **9780521859**: p. 1-372.

## Figures

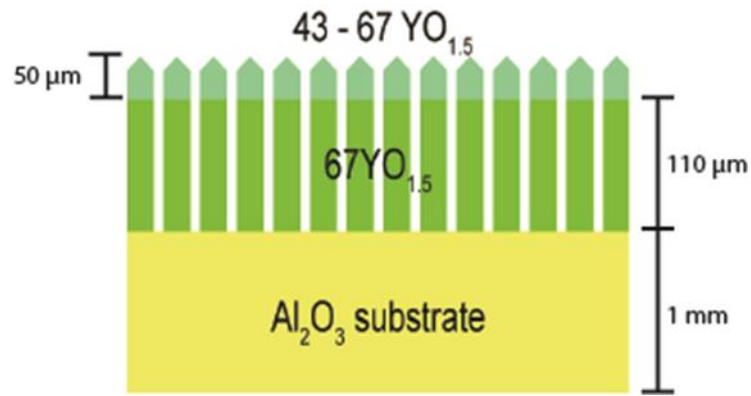


**Figure 1:** (A) Schematic representation of the jumping beam evaporation process and (B) schematic representation of the as coated TBCs used for this study.

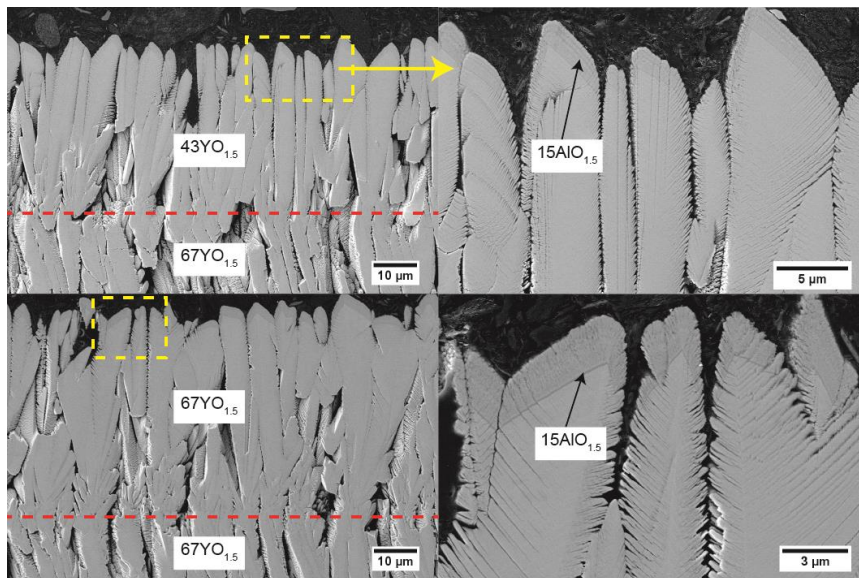


**Figure 2:** SEM cross-section image for the as coated samples from the lowest 43YO<sub>1.5</sub> content to the highest 67 YO<sub>1.5</sub> content. The dashed red line shows the interface between the underlying previously coated 67 YO<sub>1.5</sub> and the new layer. High magnification images are shown on the right side for the area delimited within the dotted yellow rectangles.

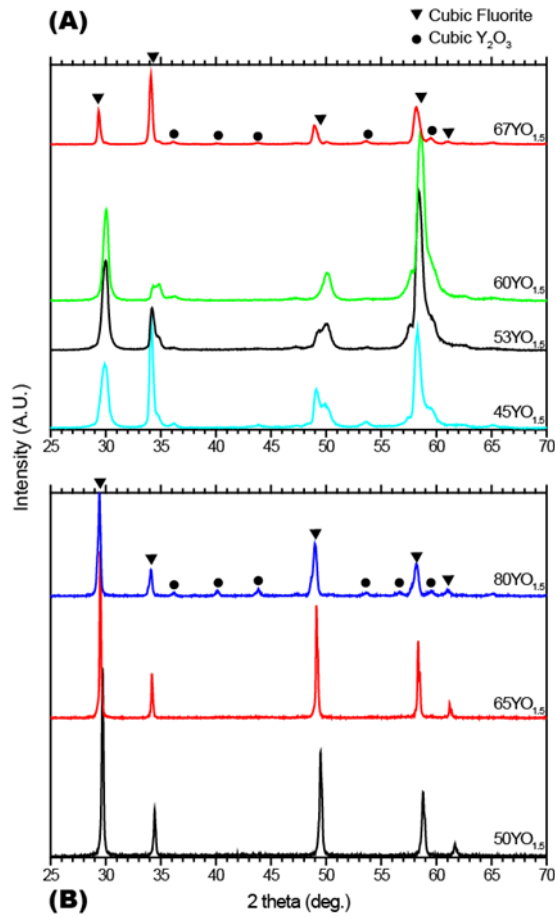


**Figure 3:** XRD plots for the (A) as coated TBCs with different YO<sub>1.5</sub> compositions and (B) as synthesized YO<sub>1.5</sub> powders.

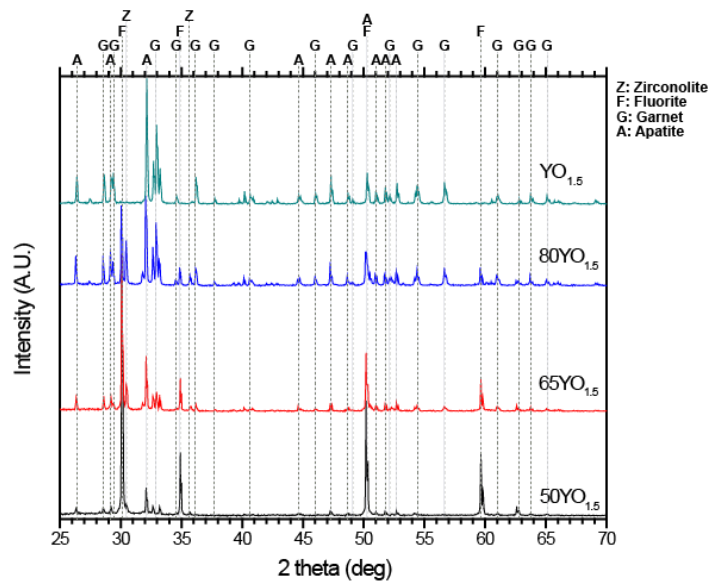


**Figure 4:** XRD plots for the YO<sub>1.5</sub>/Iceland VA mixtures heat treated for 10 h at 1250 °C.

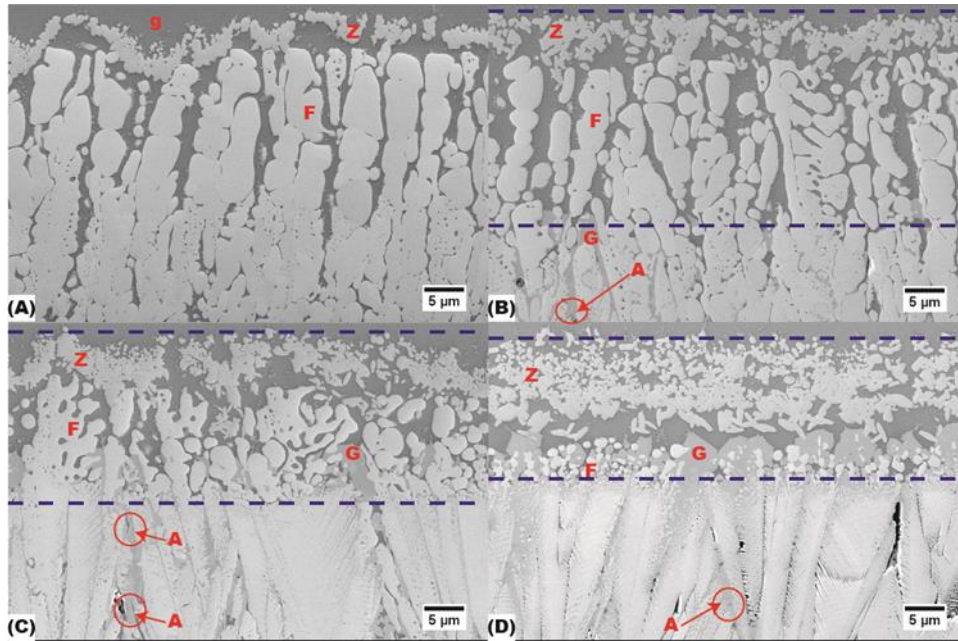


**Figure 5:** Cross-section SEM image of the reacted TBCs for 1 h at 1250 °C with Iceland VA. The area delimited within the dotted lines represent the reaction zone, “g” stands for the unreacted glass. A) shows the reaction for the 43YO<sub>1.5</sub>, B) for the 53, C) for the 60 and D) for the 67.

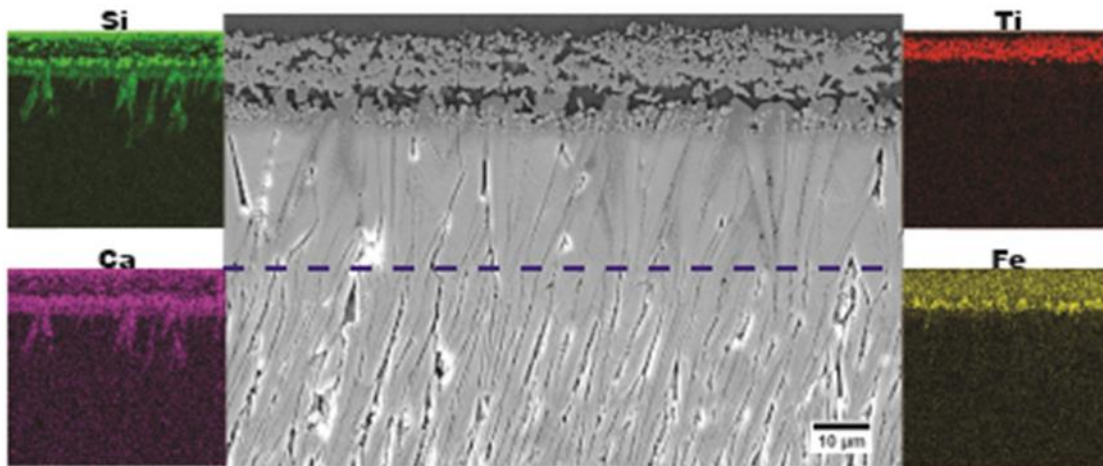


**Figure 6:** Cross-section SEM image of the infiltrated 67YO<sub>1.5</sub> TBC sample showing the elemental mapping for the overall infiltration (seen as Ca and Si mappings) and reaction layer zone with the Ti and Fe concentration. The dotted line shows the interface between the new and old deposited coatings.

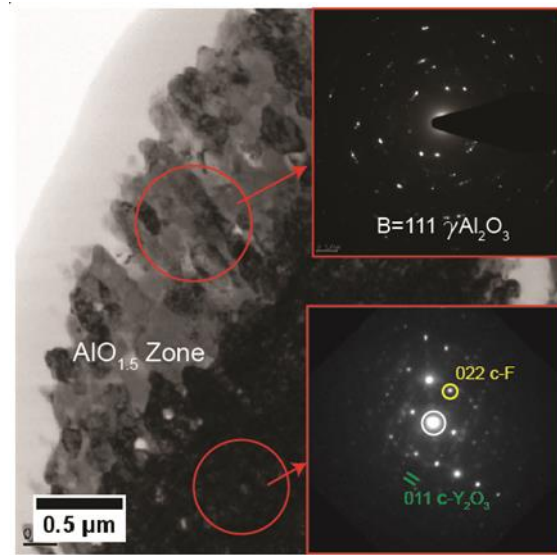


**Figure 7:** Bright field TEM image of the 67YO<sub>1.5</sub> column after 1 h heat treatment at 1250 °C from the non-infiltrated zone. The SAED images show the non-mixed alumina phases at the alumina rich zone and the mixture of cubic fluorite and cubic yttria at the core of the TBC column.

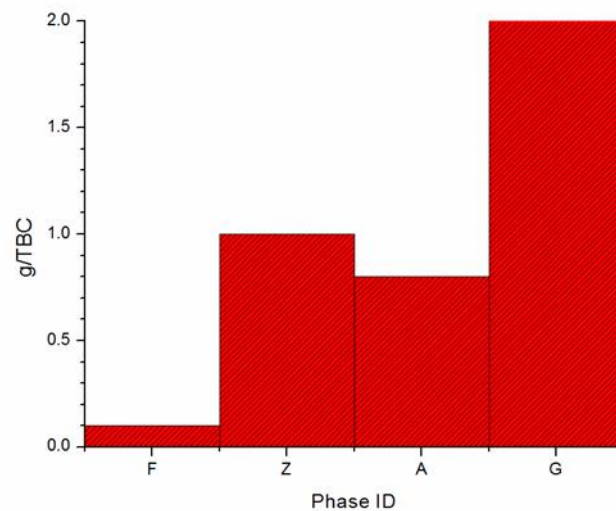


**Figure 8:** g:TBC ratio plot for the produced reaction products. Where the g represents the amount in mol % of the glass oxides and the TBC represents the YO<sub>1.5</sub> and ZrO<sub>2</sub> contents for the 67YO<sub>1.5</sub> TBC coating infiltrated for 1 h at 1250 °C.

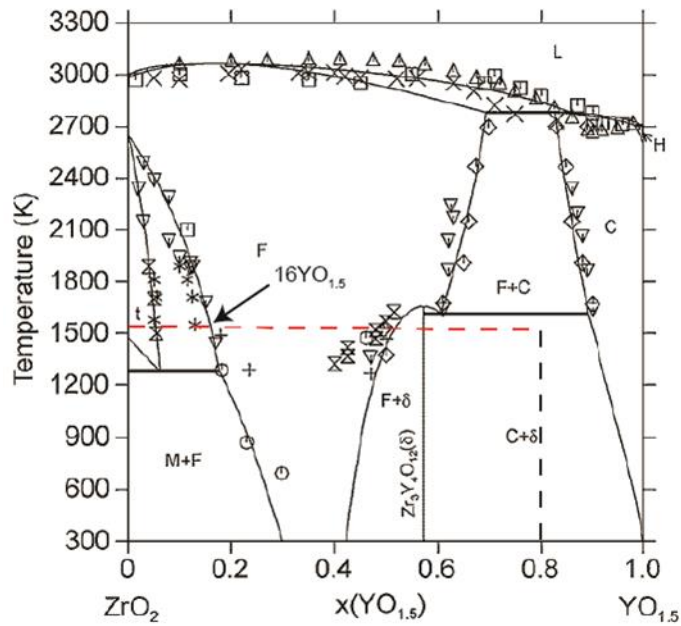


**Figure 9:** Adapted phase diagram from [55] of the  $ZrO_2$ - $YO_{1.5}$  system showing the possible phases for the tested system at 1250 °C up to 80 $YO_{1.5}$ . Single arrows represent the other powder compositions of 65 and 50  $YO_{1.5}$ .

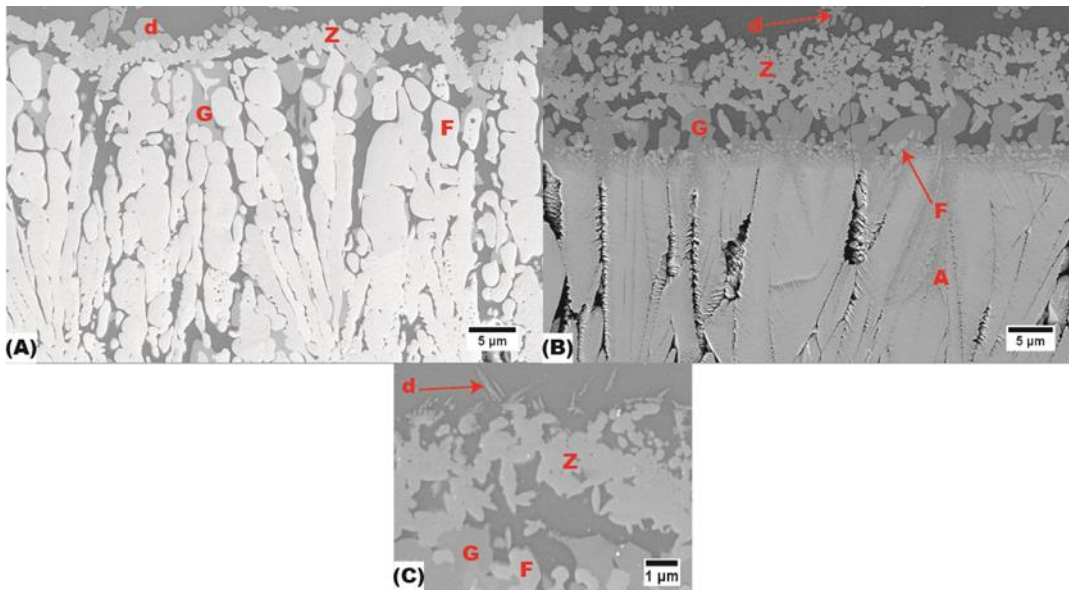


**Figure 10:** SEM image of the (A) 43 $YO_{1.5}$  TBC sample after slow cooling, (B) 67 $YO_{1.5}$  TBC sample after slow cooling and (C) 67  $YO_{1.5}$  TBC sample from the top reaction zone after air quenching showing the small dendrite particle formation. All the samples had the same infiltration time of 1 h at 1250 °C

Table list:

**Table 1:** Summary of reaction phases for the Iceland VA/ YO<sub>1.5</sub> powders heat treated for 10 h at 1250 °C. RE stands for rare-earth ion.

Phase name	ID	Theoretical formula
Apatite	A	(Ca,Mg,RE) <sub>2</sub> (RE,Zr) <sub>8</sub> (SiO <sub>4</sub> ) <sub>6</sub> O <sub>2</sub>
Garnet	G	(RE,Zr,Ca) <sub>3</sub> (Mg,Al,Fe,Ti,Zr) <sub>2</sub> (Si,Al,Fe) <sub>3</sub> O <sub>12</sub>
Fluorite	F	(RE,Zr,Ca)O <sub>1.x</sub>
Zirconolite	Z	(Ca,RE, Zr) <sub>2</sub> (Fe, Ti, Al, Mg) <sub>2</sub> O <sub>7</sub>

**Table 2:** Summary of chemical composition of reaction products and residual glass (g) for the 67YO<sub>1.5</sub> coating, measured by EDS in SEM. Unless specified in the table, the element composition error was below 1.0 mol %.

Phase ID	Chemical composition (mol %)									
	NaO <sub>0.5</sub>	MgO	AlO <sub>1.5</sub>	SiO <sub>2</sub>	KO <sub>0.5</sub>	CaO	TiO <sub>2</sub>	FeO	YO <sub>1.5</sub>	ZrO <sub>2</sub>
Z	-	1.5	3.5	3.9 ±2.5	-	2.0	19.9	19.3	21.2 ±1.3	28.7 ±1.9
G	-	6.8 ±1.1	7.2 ±2.2	20.7 ±2.2	-	9.6	0.9	21.9 ±6.5	29.4 ±5.1	3.5 ±2.3
A	-	1.7	0.4	30.7 ±3.2	-	10.4 ±1.3	-	0.6	47.8 ±2.1	8.4 ±4.7

F	-	-	-	-	-	0.6	4.5	6.7	23.5	64.8
									±2.5	±3.2
g	3.7	5.9	13.2	43.6	0.9	10.3	1.9	10.0	7.8	2.7 ±0.2